ORIGINAL RESEARCH ARTICLE

High-temperature Corrosion of ~ 30 Pct Porous FeCr Stainless Steels in Air: Long-Term Evaluation Up to Breakaway

D. KOSZELOW, M. MAKOWSKA, A. DREWNIAK, G. CEMPURA, P. JASIŃSKI, and S. MOLIN

In this work, a long-term (up to 6000 hours) corrosion evaluation of three porous (~ 30 pct of initial porosity) ferritic iron-chromium alloys with different Cr contents (20, 22, and 27 wt pct of Cr) was carried out at 600 °C, 700 °C, 800 °C, and 900 °C in air. Mass gain measurements and SEM analyses revealed that at temperatures above 600 °C, all alloys exhibit breakaway corrosion, whereas at 600 °C, none of the alloys were heavily oxidized even after 6000 hours. Based on the results, the diffusion character of the corrosion of porous chromia-forming alloys was identified. The microstructure changes at high temperatures in porous alloys containing 22 wt pct of Cr were determined in detail by transmission electron microscopy. The proposed prediction model indicated that the lifetimes of the Fe20Cr and Fe22Cr alloys were determined as 1250 hours (± 535 hours) and 1460 hours (± 640 hours), respectively. It is in agreement with the long-term oxidation experiment. For the Fe27Cr alloy, the deviation between predicted and observed lifetimes occurs. The proposed model allows for qualitative estimation of the porous alloys' lifetime with experimentally validated accuracy.

https://doi.org/10.1007/s11661-023-07005-z

I. INTRODUCTION

THE porous form of ferritic alloys (characterized by code centered cubic crystallographic structure—BCC) was proposed as a support component in solid oxide cells (SOCs).[1–3] The advantages of using porous alloys in such devices are their lower price, which allows for decreasing a cost of the whole device when compared with the SOCs that used advanced ceramic components, as well as the manufacturability of complex shapes.[4] Other possible applications of porous alloys include their use as components of gas membranes[5] and sensor systems.[6] However, use of porous iron-chromium alloys (as well as other porous alloys) at high temperatures is hindered by the limited knowledge of their oxidation properties under operating conditions.

Porous alloys have significantly larger specific surface areas than their dense forms, so the interface between the air (oxygen source) and alloy is also greater. As indicated in our previous work, the specific surface area of a porous alloy is up to 28 times larger than that of its dense form,[7] which is expected to have a tremendous impact on the corrosion kinetics. For the long-term corrosion resistance of the ferritic FeCr alloys, the most important factor is the chromium reservoir. During the high-temperature exposure, the chromium oxidizes into chromia up to the moment that there is large loss of chromium in the alloy and oxidation of Fe starts. The uncontrolled oxidation of Fe is called breakaway corrosion process. Due to the increased interface area between air and the alloy, for porous alloys, the appearance of a breakaway corrosion is expected to be faster than for the dense alloys. Nevertheless, the influence of the alloys' porosity on their corrosion resistance has not been well described yet, and there are still only a few papers on the corrosion of porous alloys.[8–14]

Stefan *et al.* demonstrated that the corrosion process of porous FeCr alloys follows the parabolic rate law, which confirms the diffusion character of the corrosion process for porous ferritic alloys (similarly to the case of

D. KOSZELOW, A. DREWNIAK, P. JASIŃSKI, and S. MOLIN are with the Advanced Materials Centre, Faculty of Electronics, Telecommunications and Informatics, Gdańsk University of Technology, 80-233 Gdańsk, Poland. Contact e-mail: damian.koszelow@pg.edu.pl M. MAKOWSKA is with the Laboratory for Nuclear Materials, Laboratory for Synchrotron Radiation and Femtochemistry, Paul Scherrer Institut, 5232 Villigen, Switzerland. G. CEMPURA is with the AGH University of Science and Technology, Faculty of Metal Engineering and Industrial Computer Science, International Centre of Electron Microscopy for Materials Science, al. Mickiewicza 30, 30-059 Krakow, Poland.

Manuscript submitted November 7, 2022; accepted February 4, 2023.

Article published online February 27, 2023

dense alloys).[11] Boccaccini *et al*. indicated the similarity of the creep mechanism between porous and dense alloys at 650 °C to 800 °C, which is important for metal-supported solid oxide fuel cell applications.[9] High creep resistance protects against electrolyte bending during operation.

To ensure a sufficient (> 10,000 hours) lifespan of devices containing components consisting of porous ferritic alloys, specific requirements, such as gas permeation and high conductivity under operating conditions, have to be fulfilled. High chromium content (usually > 16 wt pct) alloys seem to be the only good choice because of their high corrosion resistance in air and hydrogen atmospheres. Many research groups have demonstrated the use of dense forms of these alloys (such as Crofer 22 APU and Crofer 22 H by Sanergy, which contain 20 to 24 wt pct Cr) in SOC systems.[15–20] During the exposure, a slow diffusion of Cr^{3+} cations leads to the formation of a continuous passive layer of Cr_2O_3 on the alloy surface that protects the alloy from further oxidation.[21–23] The same mechanism of the corrosion process is observed for porous FeCr alloys. Although there are metal oxides with better corrosion protective properties than Cr_2O_3 (*i.e*., Al_2O_3 and SiO_2),[24–26] they cannot be used for the discussed application due to their poor electrical conductivity at high temperatures (10^{-8} to 5×10^{-3} mS cm^{-1} at 500 °C to 1000 °C for Al_2O_3 and 10^{-5} to 2×10^{-3} mS cm^{-1} at 500 °C to 1000 °C for SiO_2).[27] In contrast, chromia (Cr_2O_3) has an electrical conductivity of 1 to 10 mS cm^{-1} at 600 °C to 800 °C.[28]

Several approaches have been developed to estimate the lifespan of alloys in recent years. For instance, Huczkowski *et al*. connected the thickness of an alloy sheet with its lifespan.[29] They observed that for chromia-forming alloys, the time to the appearance of breakaway corrosion increases with the specimen's thickness. For example, the lifespan of Crofer 22 APU increases by almost 2 orders of magnitude when the thickness of the oxidized sample increases from 0.1 to 1 mm. Asensio-Jimenez *et al*. also confirmed a similar dependence.[30] On the other hand, Tucker *et al*. proposed a 3 μm thickness of oxide scale as a threshold value for estimating the lifespan of the alloy.[31] Huczkowski *et al*. showed that there is a threshold value of chromium content which provides a protective feature (~ 12 wt pct of Cr in FeCr systems).[29,32] In our previous work, a similar model for estimating the lifespan of porous Fe22Cr was proposed, and it assumed a 10 to 12 pct chromium content threshold band to reach a breakaway corrosion formation point.[7] This model took into consideration only short-term oxidation data, so it should still be verified by long-term experiments.

The porous form of high chromium FeCr alloys is considered a potential support material in SOCs. The chemical composition provides sufficient electrical conductivity for efficient current collection. The open porosity of the investigated alloy allows for gas transport through the material, which is an important feature for reactant supply to SOCs electrodes. The growing oxide consumes Cr and also decreases gas transport through the porous alloy, shortening its lifespan. To the best of our knowledge, this is the first work addressing the lifespan evaluation of the porous FeCr alloys based on long-term oxidation tests. Defining the lifespan of the porous ferritic FeCr alloys allows for the determination of the lifespan of metal-supported SOCs and gas membranes. Thus, long-term oxidation research is necessary for the creation of the lifespan prediction model of porous FeCr alloys.

This study describes an evaluation of the long-term (up to 6000 hours) corrosion process for porous FeCr alloys with different Cr contents (20 to 27 wt pct Cr) in the 600 °C to 900 °C temperature range. The obtained results were compared with the available dense alloy data. Then, the lifespan of the alloys was estimated based on information from post-mortem analyses such as mass gains and changes in the chromium level during exposure for each alloy composition.

II. EXPERIMENTAL

A. *Sample Preparation*

Porous metal sheets were sourced from Höganäs AB (experimental alloys Fe20Cr, Fe22Cr and Fe27Cr, Höganäs, Sweden). These alloys were produced from powders with a particle size fraction < 53 μm by a tape-casting process and were sintered in hydrogen (1250 °C for 30 minutes). The sintered sheets had dimensions of ~ 10 × 10 cm^2 and a thickness of ~ 0.35 mm. The composition of each investigated alloy reported by the producer is presented in Table S.1. These data were confirmed by the Inductively Coupled Plasma (ICP) spectroscopy and energy-dispersive X-ray (EDX) methods.

The initial porosity of the samples reported by the producer is 30 pct. This value was confirmed using two approaches: the Archimedes method—liquid displacement (using kerosene), and an electron microscopy image analysis using the commercial Phenom PoroMetric Software (Thermo Fisher). The porosity was determined by analyzing 20 pictures taken at a magnification of 2500× for each analyzed specimen. The error bars were calculated as a standard deviation of the mean value. The porosity was also determined *via* the image analysis method after selected time intervals for each oxidation temperature.

For the long-term oxidation experiments, the alloy sheet was cut into 1 × 1 cm squares. For the short-term thermogravimetric experiments, samples with dimensions of 1 × 2 cm were used. After cutting, the samples were cleaned in an ultrasonic bath sequentially in acetone and ethanol.

B. *Long-Term Oxidation Tests*

Long-term cyclic high-temperature oxidation was performed in a chamber furnace in an air atmosphere at 600 °C, 700 °C, 800 °C, and 900 °C. For each temperature, at least 10 specimens of each alloy were used for statistics/reproducibility. The oxidation cycles

at 600 °C, 700 °C, and 800 °C had a duration of 100 and 150 hours initially (total 250 hours) followed by cycles of 250 hours up to breakaway. For 900 °C, the cycles were 10, 20, and 70 hours, totalling 100 hours. The heating and cooling rates were 180 °C h^{-1}. The samples were periodically removed from the furnace and weighed on a microbalance (Radwag XA 5Y.M, accuracy of 1 μg, Poland). The mass gain was calculated as the relative mass change (pct) with respect to the initial sample mass. The mass gain was also recalculated to the surface specific mass gain (mg cm^{-2}), using the surface area information from our previous work (0.022 cm^2 g^{-1}, calculated from a tomographic experiment[7]).

C. *Thermogravimetric Analysis*

Short-term thermogravimetric experiments were performed using a CI Precision MK5-2 (United Kingdom) thermobalance. The oxidation time at a holding temperature of 700 °C was 300 hours and a heating rate of 180 °C h^{-1}. Measurements were carried out with an airflow rate of 30 mL min^{-1}.

The lifetimes of the porous alloys were predicted based on short-term isothermal thermogravimetric data and the methodology developed in Reference 7. For Fe20Cr and Fe27Cr, the threshold mass gain values for the appearance of breakaway corrosion were calculated as 5.1 and 8.3 pct, respectively (determined at 900 °C). Short-term mass gain curves, presented in log–log plots, were extrapolated using the linear regression method. The confidence interval was determined by the prediction band method, assuming a 95 pct confidence level. The predicted lifetime was the intersection of the fitting and the threshold mass gain values. These data were compared with the cyclic oxidation mass gains and scanning electron microscopy (SEM) micrographs of the alloys.

D. *Microscopy Analysis*

The microstructure of the samples was analyzed using scanning (SEM) and transmission (TEM) electron microscopy. A Phenom XL SEM microscope (Thermo Fisher Scientific, Netherlands) was used to observe changes on the surface and polished cross-section microstructure of the alloys. A backscatter electron detector (BSE) was used. Changes in the chemical compositions were determined by energy-dispersive X-ray spectroscopy (EDX) using an integrated analyzer (Thermo Fisher Scientific, 25 mm^2 Silicon Drift Detector).

The Cr content of the as-produced and differently oxidized alloys was calculated as the average of 15 EDX measurements carried out in different regions of the samples. The error bars were determined as the standard deviation.

The samples for the TEM investigations were prepared as lamellae. They were prepared by sputtering the sample surface with Ga^+ ions emitted from a liquid metal ion source (FIB). A thin Pt layer was deposited on the region of interest to minimize the curtain effect while thinning the sample with the ion beam. The lamellae were finished with thinning down to a level of several dozen nanometers after being mounted in a TEM-dedicated copper grid.

The TEM/STEM analyses were performed using a Cs probe-corrected Titan Cubed G2 60-300 microscope (FEI) equipped with the ChemiSTEM™ system. High-resolution STEM (HRSTEM) images were acquired using a high-angle annular dark-field (HAADF) detector.

III. RESULTS AND DISCUSSION

A. *Characterization of the Raw Porous Alloys*

The Fe20Cr, Fe22Cr, and Fe27Cr alloys have a ferritic crystallographic structure and their chemical compositions, as measured by the ICP and EDX methods, which are presented in Table I. The alloys differ mainly in the Cr and Mn content. A good correlation between the values obtained by the ICP and EDX methods was obtained. The results of both techniques are also consistent with the alloy composition provided by the manufacturer (Table S.1).

The surface and cross-section SEM images of the Fe22Cr alloy are presented in Figure 1. The surfaces of the Fe20Cr and Fe27Cr alloys were similar and are presented in Figure S.1. Figure 1(b) shows well-connected steel particles with grain boundaries. The porosity of the alloy is clearly visible. The results of the porosity measurements were similar for all alloys. Using the Archimedes method, the porosity was 30 ± 2 pct, while the porosity was determined as 29 ± 5 pct for each investigated alloy by the image analysis of the polished cross sections. Based on the image analysis, the average pore size (equivalent diameter) was ~ 11 μm, with a median pore size of ~ 7 μm (results summarized in Table S.2). No significant differences in the morphology or porosity of the alloys were observed, which justifies also using the experimentally determined specific surface area of the Fe22Cr sample for Fe20Cr and Fe27Cr alloys.

B. *Long-Term Corrosion Exposures of Porous Alloys*

The alloys were oxidized at high temperatures (600 °C, 700 °C, 800 °C, and 900 °C) in an air atmosphere to determine the properties of the corrosion kinetics. The results of the mass changes are presented in Figures 2(a) through (d).

At 600 °C, even though the oxidation time was quite substantial (6000 hours, 24 thermal cycles), the overall mass gain was low, *i.e.,* < 2 pct. A noticeable difference can be observed between the Fe20Cr and the Fe22Cr/Fe27Cr alloys. For the Fe20Cr, the first oxidation cycle (0 to 100 hours) caused a rapid ~ 1 pct mass gain, which later on developed similarly to the Fe22Cr/Fe27Cr (further ~ 1 wt pct increase). The cause for the initial mass gain is the formation of iron oxide in this initial oxidation time, as will be substantiated later.

Table I. Chemical Composition of the Alloys Obtained from the ICP and EDX Measurements

Target Composition	Fe	Analyzed Chemical Composition, Wt P				[Information from the ICP Measurement]				EDX, Wt Pct	
		Cr	Mn	Ni	Si	Ti	Co	Ca	Na	Cr	Mn
Fe20Cr	bal	20.86	0.03	0.05	0.08	0.01	0.02	0.00	0.02	20.2	0.0
Fe22Cr	bal	21.87	0.25	0.02	0.08	0.01	0.01	0.00	0.00	21.3	0.1
Fe27Cr	bal	26.77	0.33	0.01	0.08	0.01	0.01	0.04	0.00	27.6	0.2

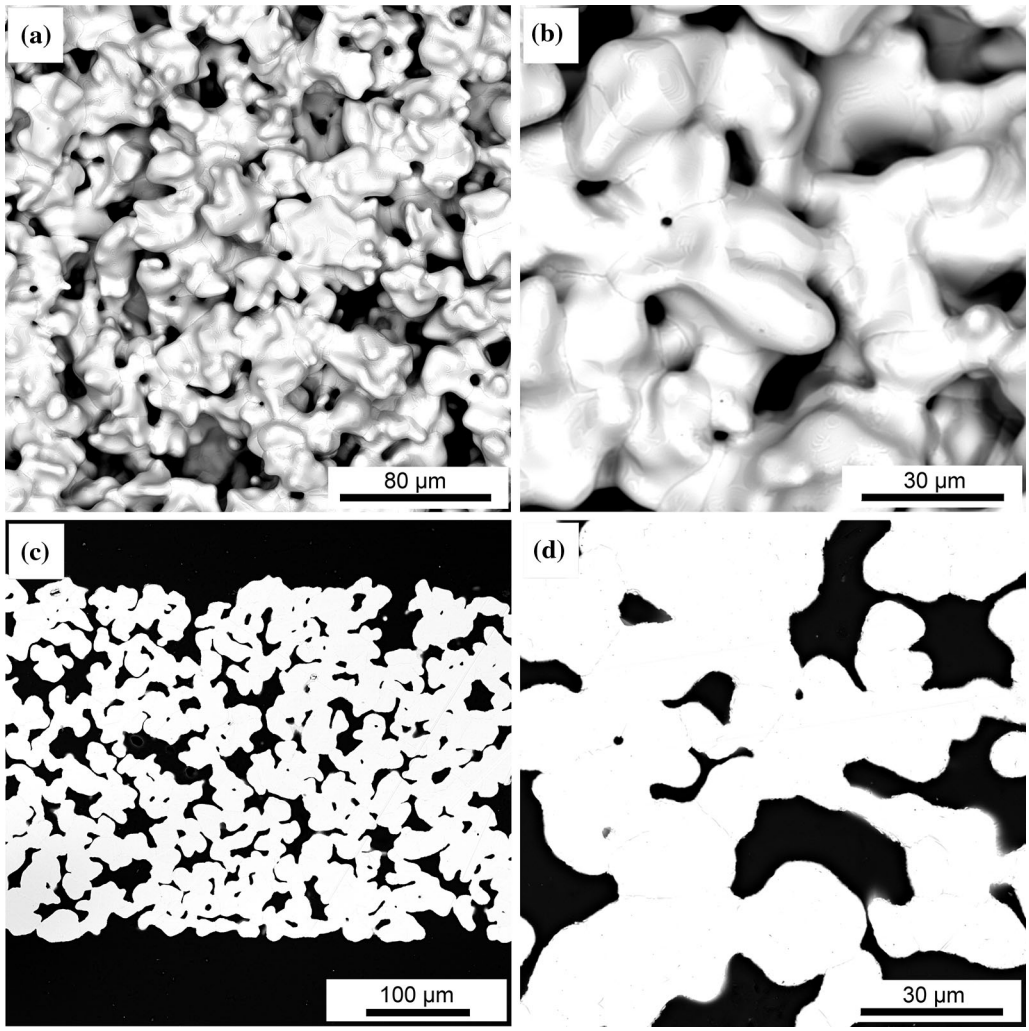

Fig. 1—SEM (backscatter electron detector) images of (*a*, *b*) surface, (*c*, *d*) cross section of the as-produced Fe22Cr alloy.

At 700 °C, the mass gain of the different alloys was similar until ~ 2000 hours, where a deviation for the Fe20Cr alloy was observed (at ~ 12 wt pct), due to the start of breakaway oxidation. At ~ 2750 hours (~ 9 pct), the Fe22Cr alloy started to increase its mass. For the Fe27Cr, with the highest Cr content, the mass gain increased steadily until ~ 4750 hours, when breakaway could be observed *via* increased mass change.

At 800 °C and 900 °C, the mass gains were much faster. At 800 °C, breakaway oxidation occurred in less than 500 hours. At 900 °C, the time to breakaway for all the alloys was < 100 hours. The mass gain data show the strong dependence on the temperature, and a dependence on the alloy Cr content.

The appearance of breakaway corrosion could be easily detected from Figures 2(b) and (c) as a change of the curve's slope. A deviation from linear dependence was clearly visible for the Fe20Cr alloy after 2000 hours of oxidation at 700 °C and after 500 hours of oxidation at 800 °C. The same behavior was observed for the Fe22Cr alloy after 3000 hours of oxidation at 700 °C and 500 hours of oxidation at 800 °C. For the Fe27Cr

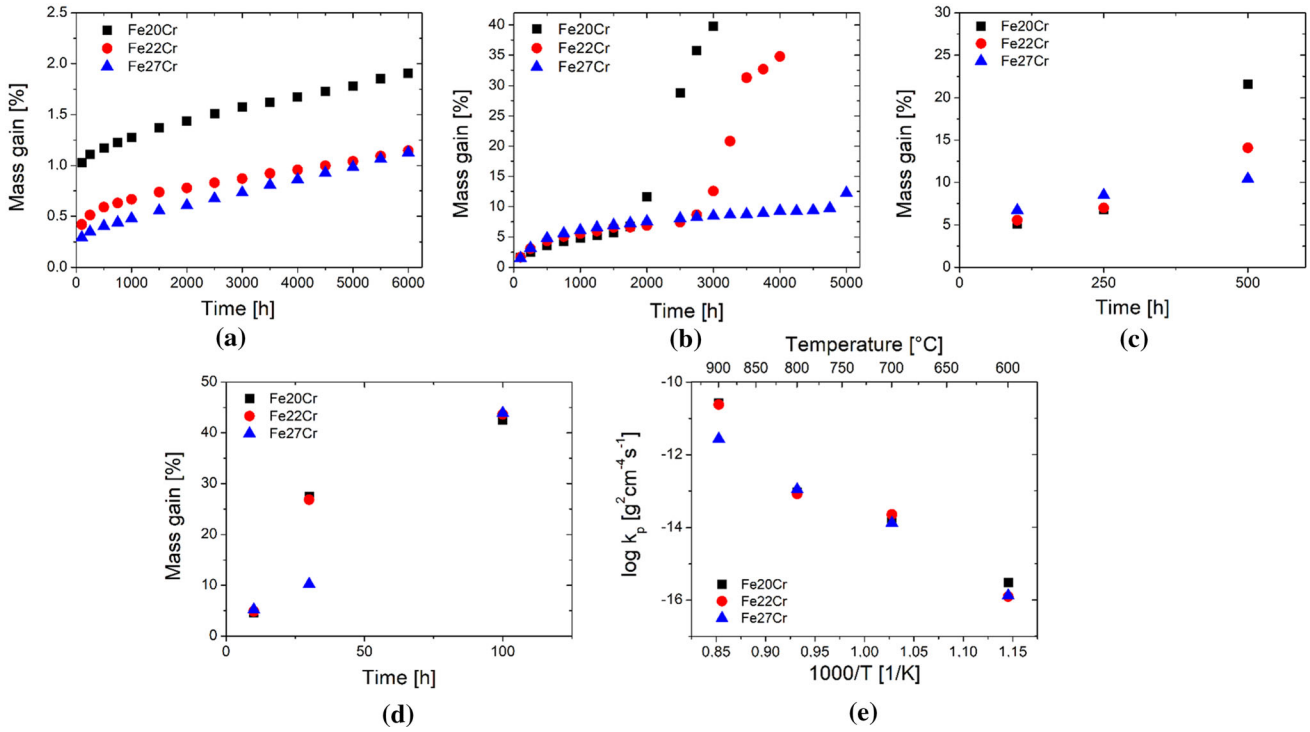

Fig. 2—Percentage mass change of oxidized Fe20Cr, Fe22Cr, and Fe27Cr alloys at (*a*) 600 °C, (*b*) 700 °C, (*c*) 800 °C, and (*d*) 900 °C. (*e*) The Arrhenius plot for Fe20Cr, Fe22Cr, and Fe27Cr alloys.

alloy, linear dependence was observed for each temperature and the first signs of breakaway corrosion appeared after 4750 hours of oxidation at 700 °C, but no trace of this was detected at 800 °C. The times that breakaway corrosion were determined to occur are based on macroscopically determined mass gain data. As studied by tomography,[33] the breakaway can occur locally in separated regions within the sample, which does not cause a large, measurable mass gain. Rough estimation of the mass gain for a totally oxidized (~ 43 wt pct mass gain) single particle of 20 μm diameter is only ~ 10 ng, so, well below the balance accuracy (~ 1 μg). Therefore, the macroscopically determined start point of the breakaway oxidation is observed with some delay and the local breakaway oxidation starts earlier. Figures S.2 and S.3 present the mass gains of the individual samples measured in each series. The scatter, which corresponds to the breakaway corrosion starting point, is noticeable. Therefore, the average breakaway oxidation start time for the set of samples has to be treated as a generalized, statistical process.

At 900 °C, the oxidation process is extremely fast. After 100 hours of oxidation, full oxidation (~ 43 wt pct mass gain) was observed for each investigated alloy. For the Fe20Cr and Fe22Cr samples, the observed mass gain was already significantly higher than for the Fe27Cr after 30 hours of oxidation, which might indicate the formation of breakaway corrosion regions for these alloys.

To determine the possible oxidation mechanism, the mass gain data were plotted in a log–log graph (Figure S.4). The mass gains follow linear curves, with a slope approaching $n \sim 0.5$, which indicates a diffusion-limited oxidation process. Typically, outward cation diffusion (Cr^{3+}) is the rate-limiting step in FeCr alloys. This mechanism can be described by the parabolic rate law using the equation:

$$\left(\frac{\Delta m}{S}\right)^2 = k_p \times t, \qquad [1]$$

where S is the surface of the alloy, Δm is a change of the alloy's mass, k_p is the parabolic rate constant, and t is the time of exposure to high-temperature conditions. Typically, the k_p values are dependent on the temperature according to the Arrhenius equation:

$$k_p = A \times \exp\left(-\frac{E_A}{RT}\right), \qquad [2]$$

which can be used to calculate the activation energy (E_A).

Based on the assumption of the parabolic kinetic law, corrosion rate constants (k_p) and activation energies (E_A) were fitted to Eqs. [1] and [2] and are summarized in Table II and presented in Figure 2(e).

The corrosion rates calculated from the parabolic rate law were similar for each alloy composition at 600 °C (1.2×10^{-16} to 3.1×10^{-16} g^2cm^{-4} s^{-1}) and at 700 °C

Table II. Corrosion Parameters After Oxidation at Different Temperatures of Fe20Cr, Fe22Cr, and Fe27Cr Alloys

Alloy	Temperature (°C)	Mass Gain @ 100 h		Mass Gain @ 1000 h (500 h for 800 °C)		Mass Gain @ 3000 h		Corrosion Rate—k_p ($g^2\ cm^{-4}\ s^{-1}$)	$k_{p\ temp}/k_{p\ 600\ °C}$	Activation Energy (eV)
		Pct	mg cm^{-2}	Pct	mg cm^{-2}	Pct	mg cm^{-2}			
Fe20Cr	600	0.9	4.5×10^{-2}	1.2	$6.0 \times \times 10^{-2}$	1.6	7.9×10^{-2}	3.1×10^{-16}	1	3.12
	700	1.6	7.9×10^{-2}	4.8	0.1	39.8	2.0	1.7×10^{-14}	55	
	800	5.1	0.3	21.6	1.1	—	—	9.3×10^{-14}	294	
	900	42.5	2.1	—	—	—	—	2.7×10^{-11}	87,097	
Fe22Cr	600	0.4	2.2×10^{-2}	0.7	3.4×10^{-2}	0.9	4.4×10^{-2}	1.3×10^{-16}	1	3.31
	700	1.7	8.3×10^{-2}	5.6	0.3	12.6	0.6	2.3×10^{-14}	177	
	800	5.6	0.3	14.1	0.7	—	—	8.3×10^{-14}	638	
	900	43.6	2.2	—	—	—	—	2.4×10^{-11}	184,615	
Fe27Cr	600	0.3	1.5×10^{-2}	0.5	2.4×10^{-2}	0.7	3.7×10^{-2}	1.3×10^{-16}	1	2.83
	700	1.5	7.5×10^{-2}	6.1	0.3	8.5	0.4	1.3×10^{-14}	100	
	800	8.5	0.3	10.4	0.5	—	—	1.1×10^{-13}	846	
	900	43.9	2.2	—	—	—	—	2.7×10^{-12}	20,769	

Table III. Chemical Composition of Regions Marked in Fig. 5 (Obtained from EDX Measurements)

Region	Cr (At. Pct)	O (At. Pct)	N (At. Pct)
1	35.7	64.3	—
2	34.7	65.3	—
3	35.8	64.2	—
4	88.0	—	12.0
5	87.9	—	11.9
6	89.4	—	10.6

(1.3×10^{-14} to 2.3×10^{-14} $g^2\ cm^{-4}\ s^{-1}$). Differences were clearly visible for higher temperatures, namely for 800 °C and 900 °C (data collected in Tables II and III). The data obtained at 800 °C correspond well to the corrosion rates obtained for dense alloys with a similar chemical composition, *e.g.*, Crofer 22 APU. Magdefrau *et al.* calculated the corrosion rate for Crofer 22 APU as 4.8×10^{-14} $g^2cm^{-4}\ s^{-1}$ at 800 °C.[16] Skilbred *et al.* determined this parameter as 5.4×10^{-14} $g^2cm^{-4}\ s^{-1}$ at 800 °C for Sandvik Sanergy HT.[34] These data are in line with the results obtained for the Fe22Cr alloy. Small changes of this parameter could be caused by compositional differences such as the Cr content or the presence of other minor alloying elements.[35]

The oxidation process before the occurrence of breakaway corrosion can be considered similar to the oxidation of dense alloys, even with more complex geometry. The complex geometry is accounted for in the limited Cr reservoir (due to the high surface-to-volume ratio), but the underlying phenomena remain the same.

As presented in Figure 2(e), the values of activation energies were similar (~ 3 eV) for each alloy. The chemical composition, *e.g.*, the different Cr contents and addition of Mn, had no visible effects on the dynamics of oxidation. The activation energy is consistent with the values reported for ferritic chromia formers. Wang *et al.* calculated the activation energy of chromium diffusion in Cr_2O_3 as 240 to 280 kJ mol^{-1} (~ 2.5 to 2.9 eV).[36] Talic *et al.* calculated the activation energy of the corrosion process for Crofer 22 APU as 310 kJ mol^{-1} (~ 3.2 eV).[37] Palcut *et al.* determined the activation energy of the same alloy as 2.6 eV.[38]

C. *Post-mortem Analysis of Porous Alloys*

1. *Scanning electron microscopy study*

SEM images of the cross sections of the heavily oxidized alloys at 800 °C and slightly oxidized at 600 °C are shown in Figure 3, whereas the images of the alloys oxidized at 700 °C, which show an intermediate oxidation stage, are presented in more detail in Figure 4. Additionally, SEM images of the surfaces of Fe20Cr, Fe22Cr, and Fe27Cr alloys after oxidation at 700 °C for 3000 hours are presented in Figure S.6 (Supplementary Material).

In the first row (Figures 3(a) through (c)), images of the Fe20Cr, Fe22Cr, and Fe27Cr alloys oxidized at 800 °C for 100 hours are presented. All samples show well-defined and distinguishable oxide scale, which was detected *via* X-Ray diffraction measurement as Cr_2O_3.[7] The XRD patterns of unoxidized Fe22Cr alloy, as well as after

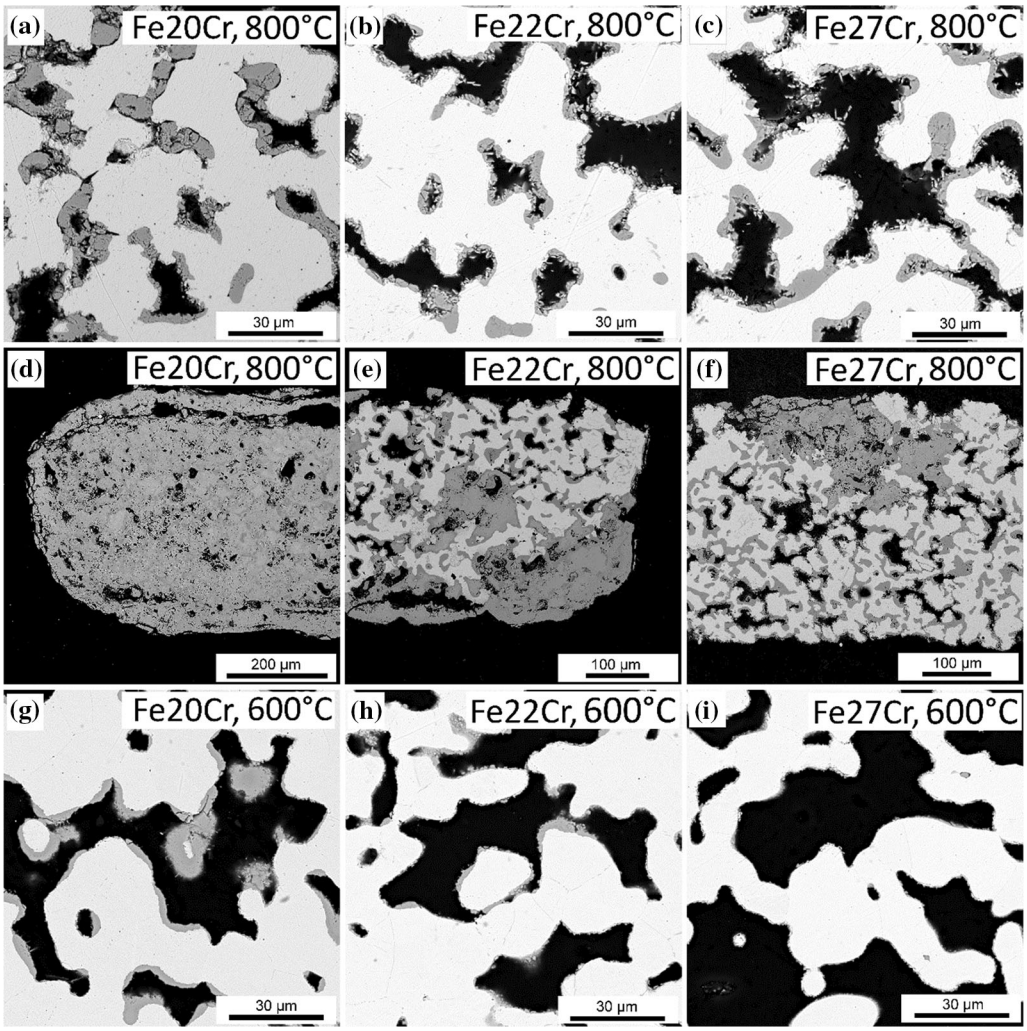

Fig. 3—SEM images of Fe20Cr (*a*, *d*, *g*), Fe22Cr (*b*, *e*, *h*), and Fe27Cr (*c*, *f*, *i*) alloys oxidized at 800 °C for 100 h (a, b, c), 500 h (d, e, f) and oxidized at 600 °C for 6000 h (g, h, i).

different steps of oxidation are also presented in Figure S.7 (Supplementary material). The Fe20Cr alloy shows the highest amount of the oxide formed, with some pores entirely filled and, therefore, exhibiting significantly reduced porosity. The oxide is severely cracked, indicating its brittleness and poor mechanical properties.

For the Fe22Cr and Fe27Cr alloys, the cross sections after 100 hours at 800 °C show similar a microstructure—a thinner layer (below 5 μm) of Cr_2O_3, when compared with the Fe20Cr alloy, was observed.

The second row of Figure 3 shows microstructures of the Fe20Cr, Fe22Cr, and Fe27Cr alloys after 500 hours of oxidation at 800 °C. The Fe20Cr alloy (Figure 3(d)) presents a fully oxidized sample with no recognizable initial morphology and porosity. The mass gain of the sample was ~ 43 pct, which confirms full oxidation of the available chromium and iron.[7] For both the Fe22Cr and Fe27Cr alloys (Figures 3(e) and (f)), the microstructures show the remaining metallic core and also some heavily oxidized regions where breakaway oxidation appeared. Most of the samples still show a retained initial porosity reduced by the formed oxide.

In contrast to oxidation at 800 °C, where breakaway oxidation for all the alloys had already occurred by 500 hours, oxidation at 600 °C had a less severe effect. Even after 6000 hours of oxidation, the oxide scale was only easily visible on the Fe20Cr sample (Figure 3(g)), whereas on the higher Cr-content alloys, it was slightly visible (Figures 3(h) and (i)). Breakaway oxidation was not observed for any of these samples. The SEM micrographs correspond well with the mass gain of the samples. For the Fe20Cr sample, the mass gain was ~ 1.8 pct whereas for both the Fe22Cr and Fe27Cr, the mass gains were ~ 1 pct. To justify the higher mass gain of the Fe20Cr, an additional EDX analysis was performed for this alloy oxidized at 600 °C for 6000 hours. The obtained chemical element maps are presented in Figure S.5 (Supplementary material). A two-phase structure consisting of iron oxide (inner layer) and chromium oxide (outer layer) can be observed in the regions around the pores. The formation of such structures could be caused by the iron oxidizing only slightly slower than the chromium at 600 °C. At higher temperatures, the chromium oxidizes significantly faster

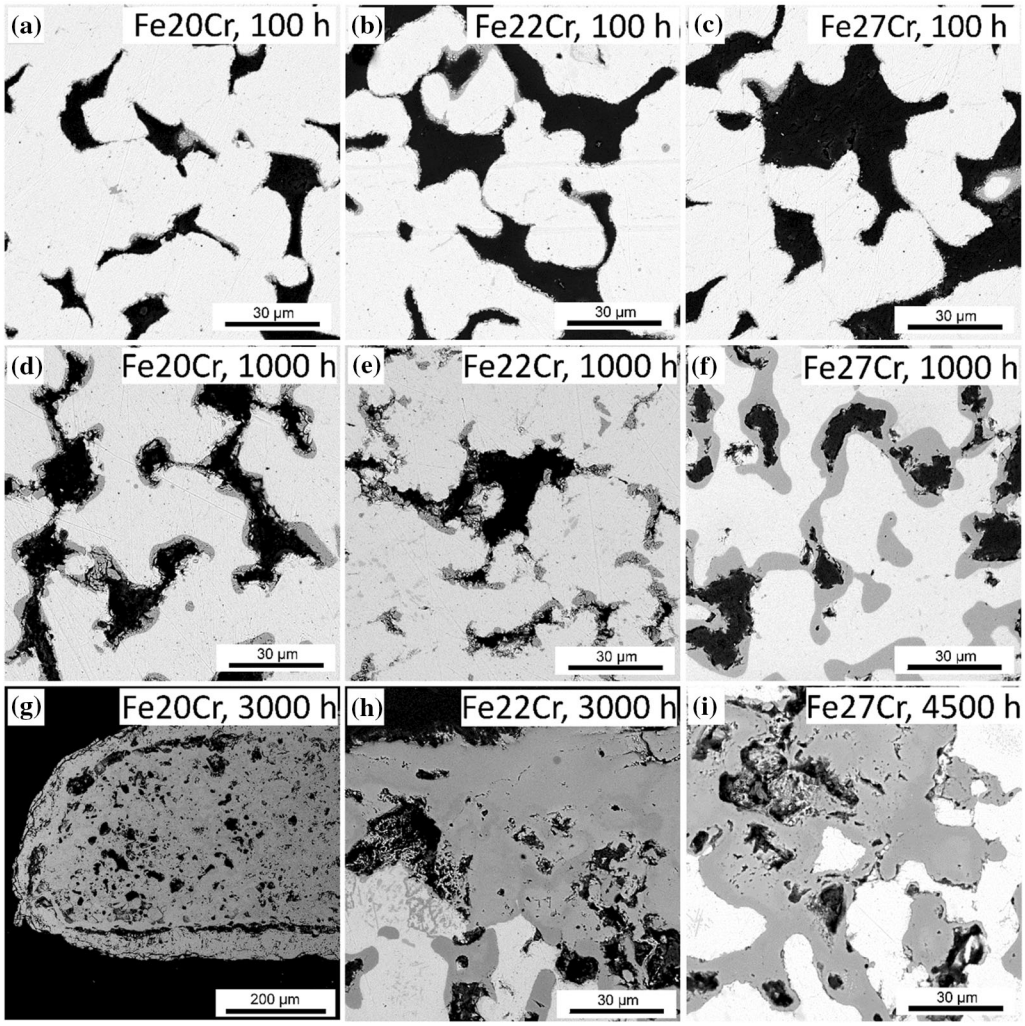

Fig. 4—SEM images of Fe20Cr (*a*, *d*, *g*), Fe22Cr (*b*, *e*, *h*) and Fe27Cr (*c*, *f*, *i*) alloys oxidized at 700 °C for 100 h (a, b, c), 1000 h (d, e, f), 3000 h (g, h), and 4500 h (i).

than the iron, so the two-phase structure is not observed in that case.

Further analysis was focused on samples oxidized at 700 °C, which seems to be the upper limit temperature for possible long-term operation of FeCr porous alloys. SEM images of the cross section of the alloys oxidized at 700 °C for different times are presented in Figure 4.

In the first row (Figures 4(a) through (c)), images of the Fe20Cr, Fe22Cr, and Fe27Cr alloys oxidized for 100 hours are shown. For each chemical composition, the oxide scale is barely visible at the surface of the particles. These micrographs correspond to an ~ 1.5 pct mass gain for each investigated sample.

The second row of Figure 4 reveals microstructures of Fe20Cr, Fe22Cr, and Fe27Cr alloys after 1000 hours of oxidation at 700 °C. For each presented sample, the oxide scale is distinguishable and limits the initial porosity (discussed later in detail), but no breakaway corrosion region was detected. The mass gain for the Fe20Cr samples after 1000 hours at 700 °C is 4.8 pct, whereas for the Fe22Cr and Fe27Cr oxidized under the same conditions, the mass gains are 5.6 and 6.1 pct, respectively.

Images of the Fe20Cr and Fe22Cr samples after 3000 hours of oxidation at 700 °C are presented in Figures 4(g) and (h), respectively. The Fe20Cr alloy (Figure 4(g)) is fully oxidized with no sign of metallic core and initial porosity, which corresponds with the ~ 40 pct mass gain. For the Fe22Cr alloy (Figure 4(h)), breakaway corrosion regions were detected but the metallic core is still visible. This result is in agreement with the mass gain plot (Figure 2(b)) that shows a deviation from the linear dependence of the mass growth after 3000 hours of oxidation at 700 °C.

In contrast to the Fe20Cr and Fe22Cr alloys, no breakaway corrosion region was identified for the Fe27Cr samples after 3000 hours of oxidation at 700 °C. After 3000 hours of oxidation at 700 °C, the mass gain for the Fe27Cr samples was ~ 8.5 pct, while for the Fe20Cr and Fe22Cr samples, it was 40 and 12.5

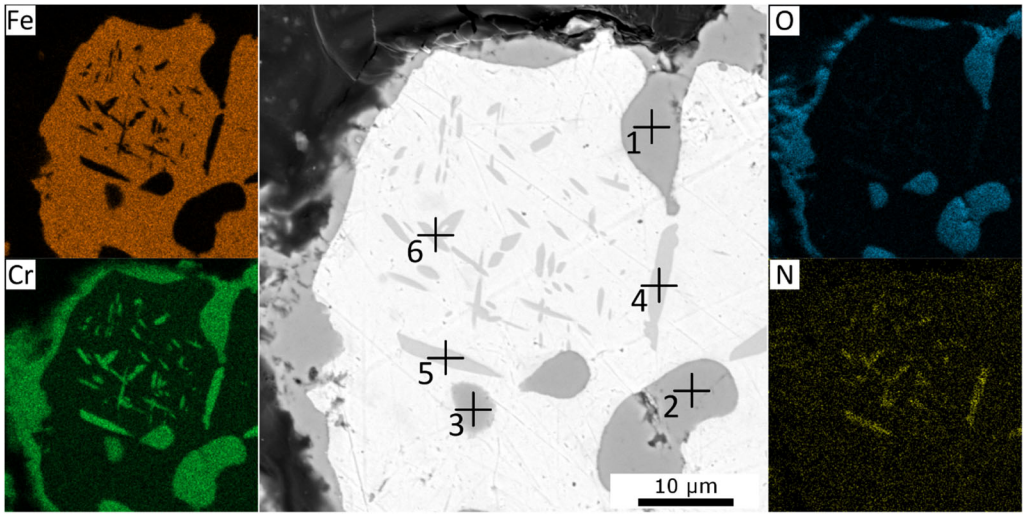

Fig. 5—EDX analysis (qualitative maps) of sample oxidized at 700 °C for 4500 h.

pct, respectively. The mass gain measurements (Figure 2(b)) for the Fe27Cr also did not show a rapid increase in the mass change.

After 4500 hours of oxidation at 700 °C, breakaway corrosion appeared for Fe27Cr alloy (Figure 4(i)), which corresponds to a 9.4 pct mass gain of the samples. It seems to be the start of the sample's accelerated oxidation, which might be caused by the appearance of breakaway corrosion only in one region of the whole sample, and thus, no rapid mass change, as observed in Figure 2(b).

2. *Internal precipitations*

Detailed analysis of the SEM images indicated the presence of internal precipitates (*e.g.,* Figure 5) in some of the particles of the Fe22Cr and Fe27Cr alloys oxidized at ≥ 700 °C. For oxidation at 600 °C, no precipitates were observed.

For the Fe20Cr alloy, which has the lowest Cr content, no formation of the precipitates was detected among the studied samples, but their formation cannot be unambiguously ruled out.

For the Fe22Cr, the precipitates were observed after oxidation at 700 °C for 3000 hours, whereas they were not visible after 1000 hours of oxidation. For oxidation at 800 °C, the precipitates were already visible after 100 hours.

For the Fe27Cr alloy, the precipitates were observed after 1000 and 100 hours for oxidation temperatures of 700 °C and 800 °C, respectively.

A typical microstructure and chemical composition of the precipitates are presented in Figure 5 based on the Fe27Cr alloy oxidized at 700 °C for 4500 hours. The darker regions inside the particles exhibit increased signal from the nitrogen and chromium elements (based on EDX). The specific elemental compositions obtained for the point measurements indicated in Figure 5 are summarized in Table III. Points 1 to 3 correspond to oxide scale—Cr_2O_3—whereas an analysis of points 4 to 6 revealed the presence of nitrogen and chromium, with no apparent oxygen signal, indicating the formation of a Cr–N phase. Due to the low concentration of N in the raw alloy, the nitrogen is believed to have diffused from the atmosphere (air) to inside the grains.

Cr_2N is a stable phase for ferritic alloys which contain less than 20 wt pct of Cr in a nitriding atmosphere in a temperature range of 500 °C to 1000 °C. Cr_2N also appears for alloys with more than 20 wt pct of Cr.[39]

Miyamoto *et al.* investigated the Fe18Cr system in a nitriding atmosphere in a temperature range of 470 °C to 670 °C. They recognized disk- and rod-shaped CrN structures and rod-shaped Cr_2N structures in the cross sections of the samples. A Cr_2N phase probably transformed into CrN during nitriding at 670 °C.[40] A mostly rod-shaped precipitated phase was observed for the samples investigated in this study.

For the samples oxidized at 700 °C and 800 °C, mixed structures of CrN and Cr_2N probably appeared. Interestingly, Bianco *et al.* indicated that purposeful controlled nitriding of the dense ferritic alloys could improve their performance when used as interconnectors in solid oxide fuel cells.[41] In our case, the samples were not prenitrided before further experiments, but spontaneous nitridation was observed during the long-term oxidation study.

Based on the limited number of analyzed samples, it seems that a higher temperature (≥ 700 °C) and higher Cr content in the alloys lead to formation of the CrN_x precipitates. The large surface area (and surface-to-volume ratio) of the porous alloys possibly also helps ensure a possible high flux of N, as similar nitridation has not been reported in the case of dense alloys with a similar chemical composition and exposed to similar conditions (*e.g.,* Crofer 22 APU oxidized up to 900 °C).

The binding of Cr by N can cause an increase in chromium consumption within the alloy, not connected to the formation of oxide scale, which can decrease the lifetime of porous ferritic alloys.

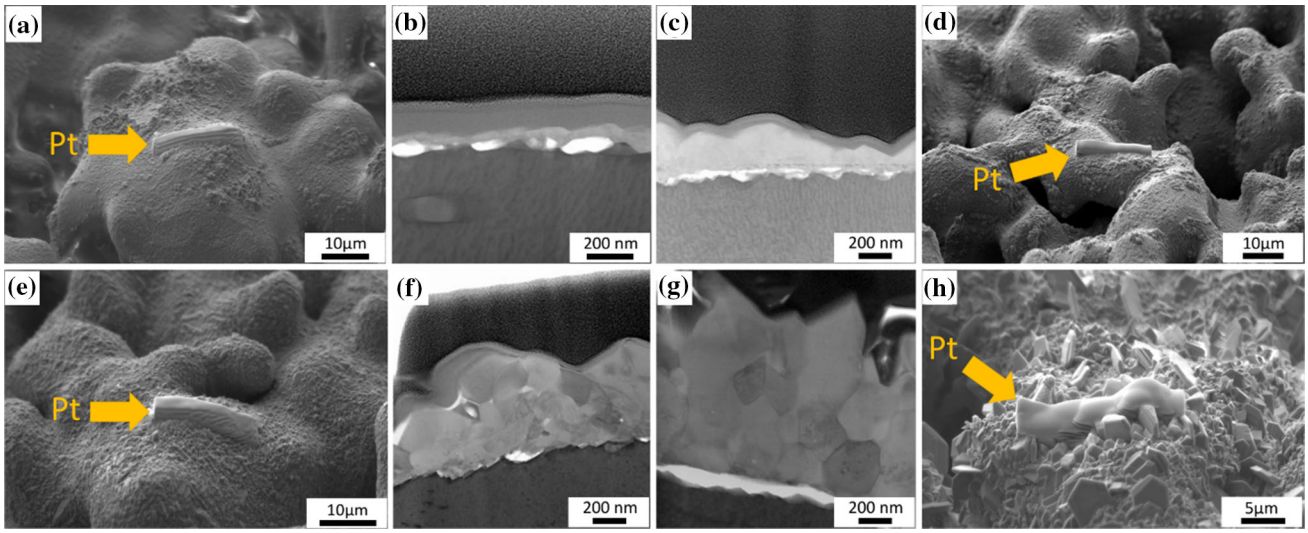

Fig. 6—SEM (surface) and STEM (FIB-lamellae cut) images of Fe22Cr alloy oxidized at (*a*, *b*) 600 °C for 3000 h; (*c*, *d*) 600 °C for 6000 h; (*e*, *f*) 700 °C for 100 h; (*g*, *h*) 700 °C for 3000 h.

3. *Transmission electron microscopy study*

Detailed characterization of the alloy-oxide was carried out on the FIB-cut lamellae by STEM. The analysis of the samples included the Fe22Cr after 3000 and 6000 hours at 600 °C and after 100 and 3000 hours at 700 °C. SEM images from the FIB-cutting process are also included. The lamellae were cut from the top parts of the particles, where the Pt cap layers are visible. The STEM images show the microstructure differences between differently oxidized samples (Figure 6).

In Figure 6(b), an alloy–oxide interface of the alloy oxidized for 3000 hours at 600 °C is presented. A thin, continuous (~ 20 to 40 nm) layer of oxide phase is visible but between the oxide and alloy phases, some voids were detected (white color). The voids in the alloy–oxide interface did not appear continuously and their widths were ~ 30 to 50 nm. After 6000 hours of oxidation at 600 °C, voids were also observed on the alloy–oxide interface (Figure 6(c)). The chromium oxide in the region close to the alloy had a fine grain structure and the further away from the alloy, the larger the oxide grains. The thickness of the discontinuous layer of voids was still about 30 to 50 nm, but the thickness of the continuous oxide scale increased to approximately 100 to 200 nm.

The changed chromium oxide grain size within the oxide scale layer was observed after 100 hours of oxidation at 700 °C (Figure 6(f)). The smallest grains were located near the alloy (about 10 to 50 nm in diameter) and the bigger grains were further away from the alloy with diameters of approximately 50 to 250 nm. The total thickness of the oxide scale was about 0.7 to 1.5 μm, which was in agreement with the analysis of the SEM images. The diameter of the voids was about 30 to 50 nm, so no changes of their size were identified in comparison with the samples oxidized at 600 °C.

After 3000 hours of oxidation at 700 °C, all grains had a similar diameter of ~ 200 to 300 μm (Figure 6(g)). There were also cracks within the oxide scale which also confirm destructive impact of the oxidation process.

The chemical composition of the lamellae was analyzed by EDX for the Fe22Cr samples oxidized at 600 °C for 6000 hours (Figure 7(a)) and at 700 °C for 3000 hours (Figure 7(b)). The results indicate that the oxide scale is composed of chromia scale. A small addition of Mn to the alloy did not result in the formation of a continuous Mn–Cr spinel layer, probably because the amount of Mn was too small (0.23 wt pct).[7] A trace of silicon (probably as a silica phase) can also be observed at the steel-chromia interface on the sample oxidized at 700 °C at 3000 hours.

4. *Chromium reservoir*

The formation of a protective chromia scale depends on the available chromium content in the bulk. Above a certain threshold value, the formation of a continuous chromia scale can be sustained, whereas below the threshold value, the oxidation of iron starts taking place, *i.e.*, as an occurrence of breakaway oxidation. Determining the threshold value of the chromium content is important for predicting the lifetime, as it defines the conditions of breakaway oxidation formation.

Huczkowski *et al.* established a threshold value of chromium content (10 wt pct) which determines the occurrence of breakaway oxidation. Our previous research[24] confirmed that this threshold value is in the range of 10 to 12 wt pct of Cr for short-term (up to 100 hours) oxidation experiments. The changes in the chromium content based on long-term oxidation research are presented in Figure 8.

For oxidation at 600 °C, even after 6000 hours, negligible changes in the chromium content were noted for all the alloys (Figure 8(a)). Barely visible microstructure changes were observed *via* SEM for samples oxidized at 600 °C, while the mass gains of these samples did not exceed 2 pct.

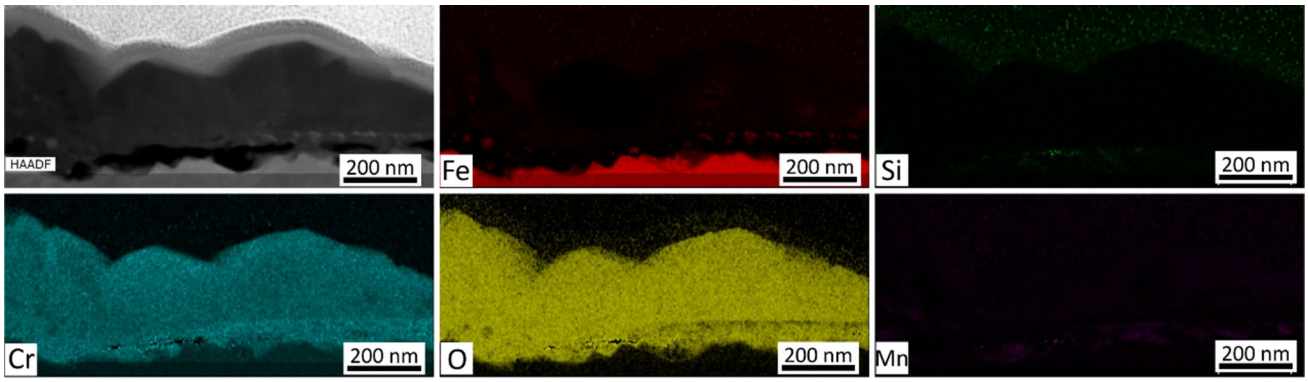

(a)

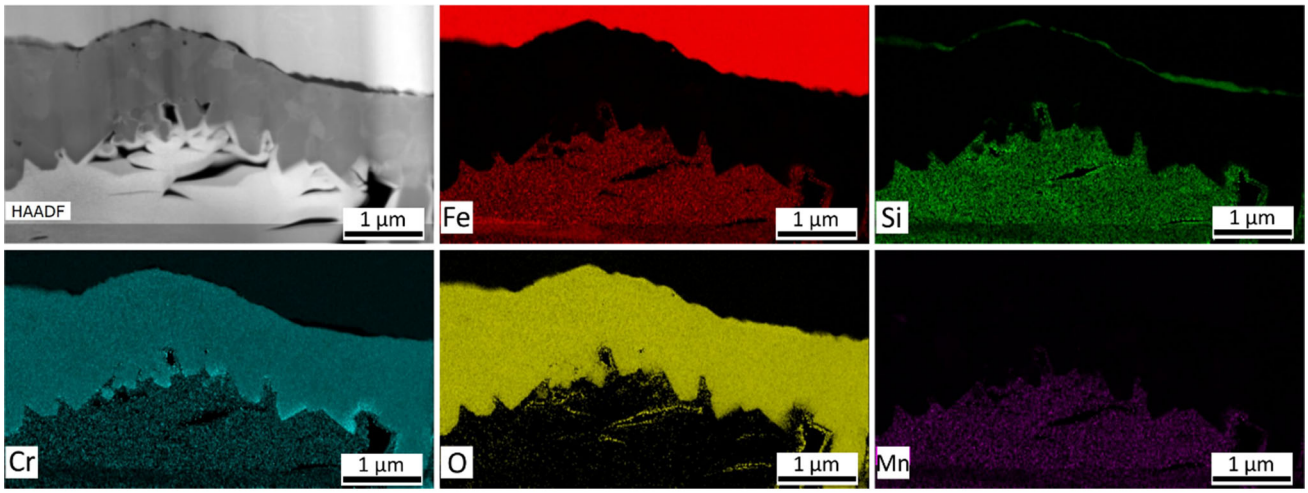

(b)

Fig. 7—EDX analysis based on TEM images for samples (*a*) oxidized at 600 °C for 6000 h, and (*b*) oxidized at 700 °C for 3000 h.

In the case of oxidation at 700 °C, changes in the chromium content were measurable (Figure 8(b)). For the Fe20Cr alloy, the level of the chromium content decreased from the initial 22 wt pct to ~ 14 pct after 1000 hours of oxidation, which is only 2 pct above the threshold band, and then after 2000 hours of oxidation, the samples were fully oxidized. For the Fe22Cr alloy, the Cr content after 3000 hours of oxidation was calculated as 12.7 pct (± 0.9 pct), which could be in the threshold band. The SEM analysis of this sample showed the formation of breakaway corrosion, but only in a few regions at the edges of the samples. For the Fe27Cr alloy, breakaway corrosion was not visible in the SEM images, and the chromium content after 3000 hours of oxidation at 700 °C was determined as 19.3 wt pct, which is definitely in the safe band.

In comparison to lower temperatures, the chromium content in the samples oxidized at 800 °C decreased faster (Figure 8(c)). Exposure for only 250 hours was sufficient for breakaway corrosion to occur in the Fe20Cr and Fe22Cr alloys. The chromium content of these alloys was 8.5 and 8.4 pct, respectively. This is consistent with the assumption that breakaway corrosion starts at ~ 12 wt pct remaining Cr in the alloy.

The Fe27Cr alloy had the highest remaining chromium content after 250 hours of oxidation at 800 °C (15.5 wt pct), which was still significantly above 12 wt pct; therefore, no breakaway corrosion was expected in this case. However, after 500 hours of oxidation at 850 °C, the remaining chromium in the Fe27Cr alloy was ~ 8.5 wt pct, which is below the threshold band and breakaway corrosion was expected to form. This is supported by the SEM analysis (Figure 3(f)) and mass gain data (Figure 2(c)), where breakaway oxidation was indeed detected.

5. *Porosity changes*

Experimentally determined porosity changes caused by the oxidation are shown in Figures 8(d) through (f) for samples oxidized at 600 °C, 700 °C, and 800 °C, respectively. A loss of porosity can lead to the functional failure of the porous element.

For the samples oxidized at 600 °C, the porosity did not change even after 6000 hours of exposure, which is consistent with the small mass gain (Figure 2(a)) and no visible microstructural changes (Figures 3(g) through (i)).

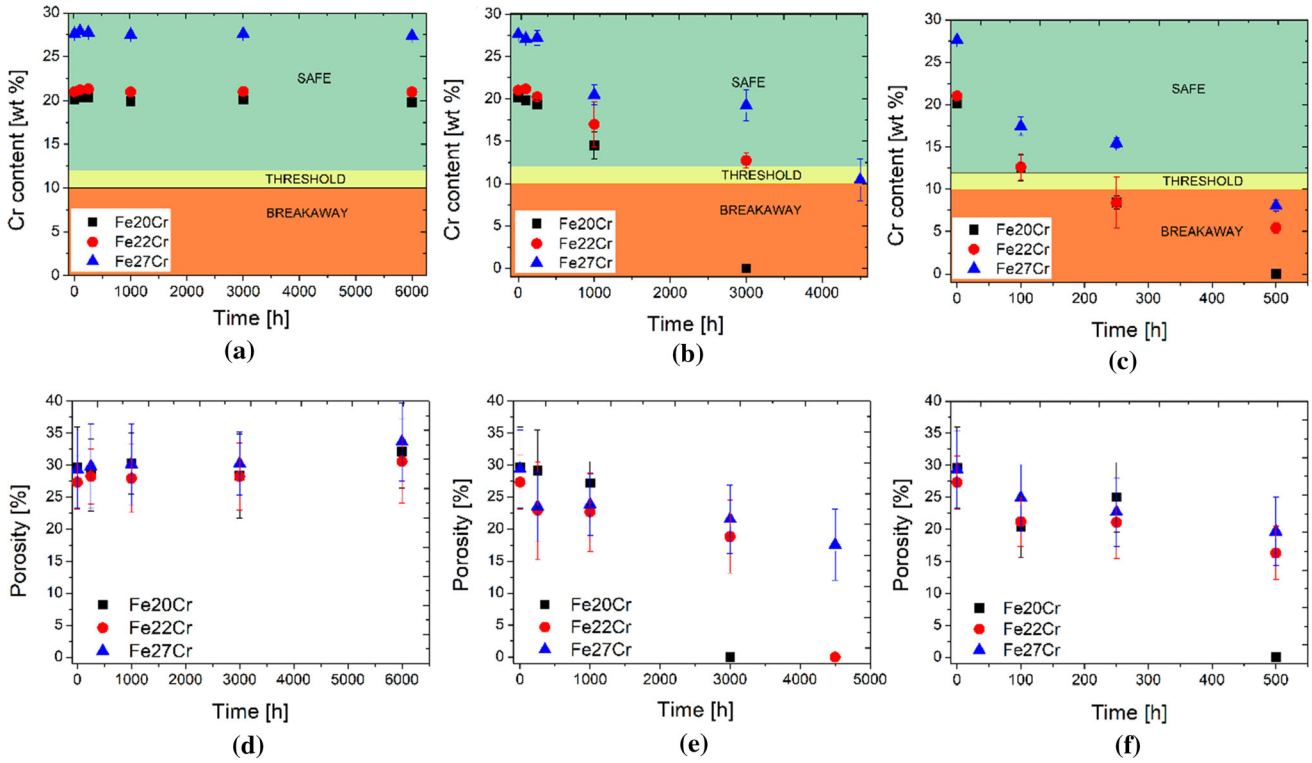

Fig. 8—Cr content in the alloy determined by EDX for Fe20Cr, Fe22Cr, and Fe27Cr alloys oxidized at (*a*) 600 °C, (*b*) 700 °C, and (*c*) 800 °C. Porosity of the samples oxidized at (*d*) 600 °C, (*e*) 700 °C, and (*f*) 800 °C.

Noticeable changes in porosity were observed for samples oxidized at 700 °C. For the Fe20Cr alloy, a small decrease in the porosity was observed during the first 1000 hours of the experiment and then a fast decrease in porosity followed. A similar, two-stage type of decrease in porosity was also observed for the Fe22Cr. Rapid porosity loss occurred after 3000 hours, which is consistent with the mass gain data and the occurrence of breakaway oxidation, as observed by SEM (Figure 4(h)). For the Fe27Cr samples, a monotonic decrease in porosity was observed up to 4500 hours.

For the samples oxidized at 800 °C, the porosity loss was more pronounced than at lower temperatures. The Fe20Cr alloy was fully oxidized after 500 hours of oxidation. For the Fe22Cr and Fe27Cr samples, a monotonic porosity loss was also observed. After 500 hours of exposure, the first indications of breakaway corrosion were observed for these samples (Figures 3(e) and (f)), which is consistent with the high mass changes—14.1 and 10.4 pct for the Fe22Cr and Fe27Cr, respectively.

D. *Lifetime Prediction of Porous Alloys*

Based on the determined threshold chromium content and oxidation kinetics data, a lifetime prediction can be established.

In our previous work, we used only short-term oxidation data for the long-term prediction. This study supplements the short-term isothermal oxidation data with a long-term cyclic oxidation validation. Moreover, in this study, changes in the chromium content were studied in a wider range of temperatures and for three alloys with different initial Cr contents, which are presented in Figures 8(a) through (c).

Isothermal (700 °C) thermogravimetric mass gain data for the alloys are presented in Figure 9. For each alloy, a threshold value of the mass gain, when breakaway corrosion should have appeared, was recalculated based on the experimentally determined value for the Fe22Cr alloy (6 wt pct).[7] Assuming that breakaway corrosion starts when the Cr content in the alloys decreases to ~ 12 wt pct (top of the threshold range, 10 to 12 wt pct), the critical Cr consumption (equivalent to a specific mass gain) can be calculated for each of the alloys. For the Fe20Cr and Fe27Cr alloys, the critical mass gain was 5.1 and 8.3 wt pct, respectively.

For the Fe20Cr and Fe22Cr alloys, the cyclic and isothermal mass gains show good agreement. The prediction model indicated that the lifetimes of the Fe20Cr and Fe22Cr alloys were determined as 1250 hours (± 535 hours) and 1460 hours (± 640 hours), respectively. Even though the relative error of the predicted alloy's lifetime seems to be relatively high, an assumed prediction band is determined for the log–log scale plot, resulting in artificially high values of the relative error. The extrapolated curves for the Fe20Cr and Fe22Cr are in line with the experimentally measured mass gains, as presented in Figures 9(a) and (b).

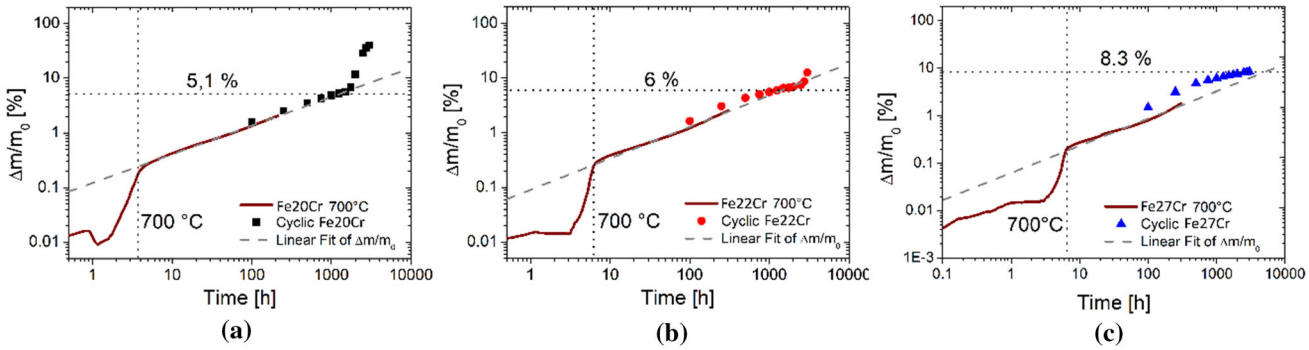

Fig. 9—Linear extrapolation of thermogravimetric data for (*a*) Fe20Cr alloy, (*b*) Fe22Cr alloy, and (*c*) Fe27Cr alloy. For each chemical composition, a threshold level of chromium content and cyclic weight measurements were also plotted.

The experimentally determined times when breakaway corrosion appears are < 1750 and 2750 hours for the Fe20Cr and Fe22Cr alloys, respectively. The model seems to underestimate the lifetime of the alloys.

The breakaway oxidation time observed as a change of the slope for the mass gain data could be misleading, as proved by a comparison of the thermogravimetric plot for the Fe27Cr oxidized at 700 °C (Figure 2(b)) and a SEM image (Figure 4(i)). The mass gain measurements reveal the occurrence of breakaway corrosion with a delay of a few hundred hours. The lifetime prediction obtained from the proposed model seems to be more accurate and better reflects the real lifetime of porous alloys. Such difference in the estimated lifetime based on the mass gain measurements and real lifetime was also proven by the SEM and tomography studies.[33]

For the Fe27Cr alloy, the cyclic and isothermal mass gain data show a visible difference. The cyclic measurements provide an 8.3 wt pct mass gain after 3000 hours, but the predicted lifetime of the alloy is about 5070 hours (± 2740 hours).

For the Fe27Cr alloy, breakaway corrosion did not appear after 3000 hours of oxidation at 700 °C. It was observed after 4500 hours of oxidation at 700 °C. The shorter lifetimes provided by the prediction model could be caused by the log–log scale effect. The relative distance between 1000 and 2000 hours in the log–log plot was small, so the calculated lifetimes could be disturbed.

The main goal of the applied prediction model was a rough estimation of lifetimes of he alloys. Additionally, the best way to predict the lifetime of a porous alloy was to consider the chromium content data, mass gains, and microscopy analysis.

IV. CONCLUSIONS

In this work, the lifetime of porous FeCr alloys was predicted based on a long-term (up to 6000 hours) corrosion evaluation in a wide temperature range (600 °C to 900 °C). Alloys with a similar microstructure, but different chemical compositions (Fe20Cr, Fe22Cr, Fe27Cr) were studied. The main difference was the chromium content, which is a key factor in determining the lifetimes of the alloys.

Oxidation at 600 °C did not cause severe degradation of any of the alloys. The oxide growth rate was low (~ 10^{-16} g^2 cm^{-4} s^{-1}) and did not change the chemical composition due to Cr consumption, nor modifies the porous structure of the alloy by filling of pores by oxidation products. Oxidation at 700 °C was characterized by an increased oxide growth rate (~ 10^{-14} g^2 cm^{-4} s^{-1}), which caused a visible alteration of the properties of the samples. For the oxidation at 800 °C, rapid growth of oxide scale was observed (~ 10^{-13} g^2 cm^{-4} s^{-1}).

The initial porosity of the samples decreased from the initial 30 pct during exposure, except for the samples oxidized at 600 °C. These results are consistent with the Cr consumption analysis. The Cr level for the samples oxidized at 700 °C and 800 °C decreased, but was constant for the samples oxidized at 600 °C. The long-term results confirmed that, for the samples consisting of 12 wt pct of Cr (or below), the formation of breakaway corrosion was detected *via* SEM imaging.

A comparison of the mass gain data with SEM micrographs indicated that determining the formation of breakaway corrosion based on a change in the slope of the thermogravimetric data can be misleading. The SEM images of the Fe27Cr alloy oxidized at 700 °C for 4500 hours revealed the occurrence of breakaway corrosion (Figure 4(i)), but no changes in the slope in the mass gain plot (Figure 2(b)) were observed. The time of the formation of breakaway corrosion estimated based on the mass gain plot should be decreased by a few hundred hours.

An analysis of the mass gains, SEM and TEM images, and thermogravimetric data in the context of predicting the lifetime of a porous alloy confirmed that an assumed 9 wt pct of chromium content in the alloy was the limit value that determined the appearance of breakaway corrosion (independently of the alloy's chemical composition). The applied prediction model made it possible to roughly estimate each alloy's lifetime and confirmed the diffusion character of the corrosion process for porous alloys. The lifetime prediction was compared with the long-term experimental oxidation results. The

convergence of these data proved the concept of estimating the lifetime of porous alloys based only on short-term results. The model seems to accurately predict the lifetime of the alloys, more precisely than can be evaluated based on the average mass gain data.

To sum up, the corrosion process for porous alloys was revealed to be limited by a diffusion process (slope of the mass gain plots). The alloy's lifetime depended on its chemical composition—the more chromium in the 'raw' alloy, the longer the lifespan. Such porous alloys can be considered promising materials for high-temperature applications, especially at 600 °C, where a long lifetime can be achieved.

ACKNOWLEDGMENTS

This project was supported by the National Science Centre Poland (NCN) Sonata Bis 8 project number 2018/30/E/ST8/00821, ''High-temperature corrosion studies and development of oxidation lifetime model of alloy powders and sintered porous alloys: effects of composition and microstructure.''

FUNDING

This project has received funding from the European Union's Horizon 2020 research and innovation programme under Grant Agreement No 823717 – ESTEEM3.

CONFLICT OF INTEREST

On behalf of all authors, the corresponding author states that there is no conflict of interest.

OPEN ACCESS

SUPPLEMENTARY INFORMATION

The online version contains supplementary material available at https://doi.org/10.1007/s11661-023-07005-z.

REFERENCES

1. J.C.W. Mah, A. Muchtar, M.R. Somalu, and M.J. Ghazali: *Int. J. Hydrogen Energy*, 2017, vol. 42, pp. 9219–29.
2. R. Wang, Z. Sun, J.-P. Choi, S.N. Basu, J.W. Stevenson, and M.C. Tucker: *Int. J. Hydrogen Energy*, 2019, vol. 44, pp. 25297–25309.
3. M.A. Hassan, O. Bin Mamat, and M. Mehdi: *Int. J. Hydrogen Energy*, 2020, vol. 45, pp. 25191–25209.
4. Z. Yang: *Int. Mater. Rev.*, 2008, vol. 53, pp. 39–52.
5. J.A. Glasscock, L. Mikkelsen, Å.H. Persson, G. Pećanac, J. Malzbender, P. Blennow, F. Bozza, and P.V. Hendriksen: *Solid State Ionics*, 2013, vol. 242, pp. 33–44.
6. Y.H. Xiang, L.Z. Liu, J.C. Shao, and H.J. Jin: *Acta Mater.*, 2020, vol. 186, pp. 105–15.
7. D. Koszelow, M. Makowska, F. Marone, J. Karczewski, P. Jasinski, and S. Molin: *Corros. Sci.*, 2021, vol. 189, 109589.
8. Y. Matus, L. Dejonghe, C. Jacobson, and S. Visco: *Solid State Ionics*, 2005, vol. 176, pp. 443–49.
9. D.N. Boccaccini, H.L. Frandsen, B.R. Sudireddy, P. Blennow, Å.H. Persson, K. Kwok, and P. Vang Hendriksen: *Int. J. Hydrogen Energy*, 2014, vol. 39, pp. 21569–80.
10. G. Reiss, H.L. Frandsen, W. Brandstätter, and A. Weber: *J. Power Sources*, 2015, vol. 273, pp. 1006–15.
11. E. Stefan, C. Denonville, Y. Larring, M. Stange, and R. Haugsrud: *Corros. Sci.*, 2020, vol. 164, 108335.
12. M. Mokhtari, T. Wada, C. Le Bourlot, J. Duchet-Rumeau, H. Kato, E. Maire, and N. Mary: *Corros. Sci.*, 2020, vol. 166, 108468.
13. S. Molin, B. Kusz, M. Gazda, and P. Jasinski: *J. Power Sources*, 2008, vol. 181, pp. 31–37.
14. X. Cai, Y. Liu, X. Wang, X. Jiao, J. Wang, F. Akhtar, and P. Feng: *Metall. Mater. Trans. A Phys. Metall. Mater. Sci.*, 2018, vol. 49, pp. 3683–91.
15. B. Öztürk, A. Topcu, S. Öztürk, and Ö.N. Cora: *Int. J. Hydrogen Energy*, 2018, vol. 43, pp. 10822–33.
16. N.J. Magdefrau, L. Chen, E.Y. Sun, and M. Aindow: *J. Power Sources*, 2013, vol. 241, pp. 756–67.
17. P. Alnegren, M. Sattari, J. Froitzheim, and J.E. Svensson: *Corros. Sci.*, 2016, vol. 110, pp. 200–12.
18. H. Shahbaznejad and H. Ebrahimifar: *J. Mater. Sci. Mater. Electron.*, 2021, vol. 32, pp. 7550–66.
19. W.N. Liu, X. Sun, E. Stephens, and M.A. Khaleel: *J. Power Sources*, 2009, vol. 189, pp. 1044–50.
20. B. Timurkutluk, S. Toros, S. Onbilgin, and H.G. Korkmaz: *Int. J. Hydrogen Energy*, 2018, vol. 43, pp. 14638–47.
21. A. Meharwal, M. Kumar, S.K. Karak, J.D. Majumdar, and I. Manna: *Metall. Mater. Trans. A Phys. Metall. Mater. Sci.*, 2020, vol. 51, pp. 5257–67.
22. B.V. Mahesh, R.K. Singh Raman, and C.C. Koch: *Metall. Mater. Trans. A Phys. Metall. Mater. Sci.*, 2015, vol. 46, pp. 1814–24.
23. V.G. Efremenko, Y.G. Chabak, A. Lekatou, A.E. Karantzalis, and A.V. Efremenko: *Metall. Mater. Trans. A Phys. Metall. Mater. Sci.*, 2016, vol. 47, pp. 1529–43.
24. J. Masalski, J. Gluszek, J. Zabrzeski, K. Nitsch, and P. Gluszek: *Thin Solid Films*, 1999, vol. 349, pp. 186–90.

25. A.M. Lazar, W.P. Yespica, S. Marcelin, N. Pébère, D. Samélor, C. Tendero, and C. Vahlas: *Corros. Sci.*, 2014, vol. 81, pp. 125–31.
26. G. Ruhi, O.P. Modi, A.S.K. Sinha, and I.B. Singh: *Corros. Sci.*, 2008, vol. 50, pp. 639–49.
27. P. Pavlasek, J. Rybař, S. Ďuriš, and J. Palenčar: *Meas. Sci. Rev.*, 2019, vol. 19, pp. 209–12.
28. A. Holt and P. Kofstad: *Solid State Ionics*, 1994, vol. 69, pp. 137–43.
29. P. Huczkowski, V. Shemet, J. Piron-Abellan, L. Singheiser, W.J. Quadakkers, and N. Christiansen: *Mater. Corros.*, 2004, vol. 55, pp. 825–30.
30. C. Asensio-Jimenez, L. Niewolak, H. Hattendorf, B. Kuhn, P. Huczkowski, L. Singheiser, and W.J. Quadakkers: *Oxid. Met.*, 2013, vol. 79, pp. 1–4.
31. M.C. Tucker: *Int. J. Hydrogen Energy*, 2020, vol. 45, pp. 24203–18.
32. P. Huczkowski, N. Christiansen, V. Shemet, J. Piron-Abellan, L. Singheiser, and W.J. Quadakkers: *J. Fuel Cell Sci. Technol.*, 2004, vol. 1, pp. 30–34.
33. D. Koszelow, S. Molin, J. Karczewski, F. Marone, and M. Makowska: *Mater. Des.*, 2022, vol. 215, 110492.
34. A.W.B. Skilbred and R. Haugsrud: *J. Power Sources*, 2012, vol. 206, pp. 70–76.
35. J.W. Fergus: *Mater. Sci. Eng. A*, 2005, vol. 397, pp. 271–83.
36. Y. Wang, Y. Liu, H. Tang, W. Li, and C. Han: *Trans. Nonferrous Met. Soc. China (English Ed.)*, 2017, vol. 27, pp. 1558–68.
37. B. Talic, S. Molin, P.V. Hendriksen, and H.L. Lein: *Corros. Sci.*, 2018, vol. 138, pp. 189–99.
38. M. Palcut, L. Mikkelsen, K. Neufeld, M. Chen, R. Knibbe, and P.V. Hendriksen: *Corros. Sci.*, 2010, vol. 52, pp. 3309–20.
39. B. Mortimer, P. Grieveson, and K.H. Jack: *Scand. J. Metall.*, 1972, vol. 1, pp. 203–09.
40. G. Miyamoto, A. Yonemoto, Y. Tanaka, T. Furuhara, and T. Maki: *Acta Mater.*, 2006, vol. 54, pp. 4771–79.
41. M. Bianco, S. Poitel, J.E. Hong, S. Yang, Z.J. Wang, M. Willinger, R. Steinberger-Wilckens, and J. Van Herle: *Corros. Sci.*, 2020, vol. 165, 108414.